Supplementary Information

Harnessing wave diffraction with metamaterial noise barriers for enhanced sound attenuation

Jieun Yang[1,†], Pyung-Sik Ma[2,†]

[1] Department of Precision and Microsystems Engineering, Faculty of Mechanical Engineering, Delft University of Technology, 2628 CD Delft, The Netherlands

[2] Department of Mechanical Engineering, Gachon University, Seongnam 13120, Republic of Korea

[†] Corresponding authors.
Email addresses: jieun.yang@tudelft.nl (J. Yang), psma@gachon.ac.kr (P.-S. Ma)

S1. Detailed information on the numerical simulation

All simulations were performed using the commercial finite element method (FEM) solver, COMSOL Multiphysics v6.3.

Wave fields around the barrier and insertion loss

To simulate the wave fields around the barrier and compute the insertion loss (IL), the noise barrier was placed at the center of a large rectangular air domain, as shown in Figure S1. The mass density $\rho_0 = 1.21$ kg/m^3 and speed of sound in air $c_0 = 343$ m/s were used. This air domain was surrounded by perfectly matched layers on all sides except the ground surface, which was modeled as a rigid boundary. 'Sound Hard Boundary' conditions were applied to all barrier surfaces as well as the ground. For the metabarrier, the neck, the air cavity, and small domain in front of the barrier surfaces are modelled by using 'Thermoviscous Acoustics' module to account for the viscous and thermal losses. In the Thermoviscous Acoustics module, 'No slip' boundary condition was applied on all boundaries. For the simulation of 'no-dissipation case' discussed in Section 3.4 of the main manuscript, this Thermviscous Acoustics module was disabled. Incident plane waves propagating parallel to the ground are modelled by using the 'Background Pressure Field'. All computational domains were meshed with a maximum element size smaller than one-sixth of the minimum wavelength across the frequency range of interest. Simulations were conducted using a Frequency Domain study within the specified frequency range. Total acoustic pressure values were extracted at receiver locations to calculate the IL values.

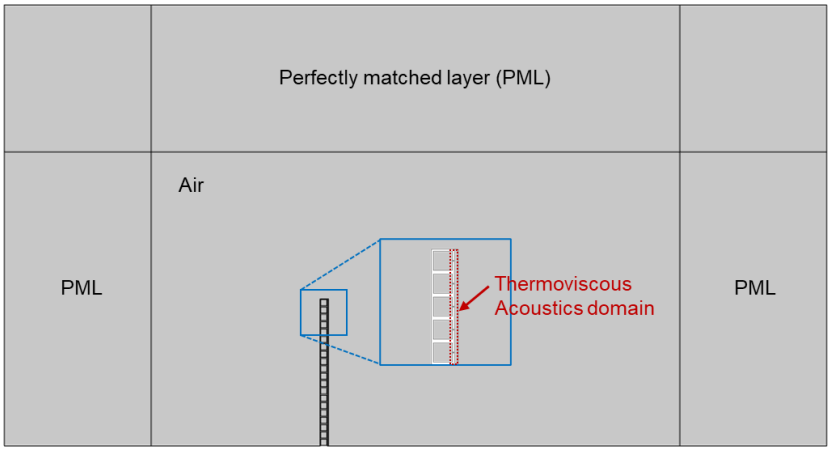

Figure S1. Numerical simulation setup used to calculate the acoustic wave fields around the barrier and insertion loss (IL) values.

Dispersion curve

The dispersion curves presented in Figure 2(b) were obtained using eigenfrequency analysis. A single unit resonator with an air domain of finite height was modeled, as shown in Figure S2(a). Periodic boundary conditions with Floquet periodicity were applied to the sides of the resonator and air domain, while all remaining boundaries were assigned Sound Hard Boundary conditions. Due to the finite height of the air domain, additional eigenmodes corresponding to resonance modes confined within the air region, which are irrelevant to the surface wave modes of interest, also appear in the results. Examples of such modes are shown in Figure S2(b). These spurious modes can be identified and filtered out during post-processing.

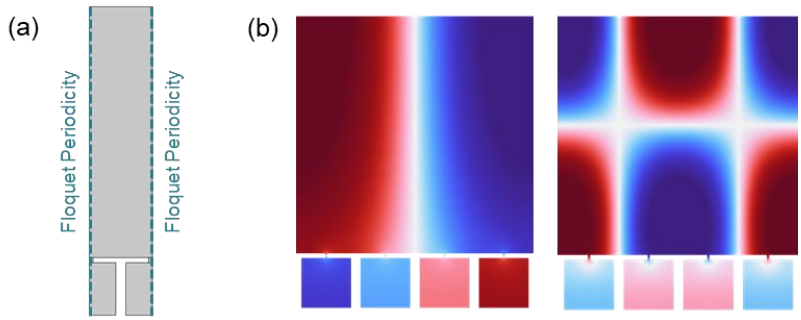

Figure S2. (a) Numerical simulation setup for the eigenvalue analysis.
(b) Examples of spurious modes confined in the finite-height air domain.

Sound absorption

To calculate the sound absorption coefficients presented in Figure 2(e) and Figure 5(b) of the main manuscript, a single resonator unit with a finite-height air domain as in Figure S2(a) was considered. The 'Plane Wave Radiation' boundary condition with an incident pressure field was applied to the top boundary of the air domain. The dissipation effects within the resonator neck were incorporated using the Thermoviscous Acoustics module, consistent with the approach used in the full barrier simulations.

S2. Influence of material properties

The numerical simulations presented in the main manuscript were performed under the assumption that the noise barrier structures are acoustically rigid, modeled as hard wall boundaries without considering the material properties of the barrier itself. To evaluate the influence of structural

material properties on the acoustic performance, we conducted additional simulations in COMSOL Multiphysics that incorporate acoustic-structure interaction. These simulations account for the coupling between acoustic waves in air and the structural response of the noise barriers.

Two materials were considered: (1) the 3D printing material used in Section 5 (Experimental demonstration) of the main manuscript, a plastic material characterized by a density of ρ = 1170 kg/m^3, Young's modulus E = 2.56 GPa, Poisson's ratio v = 0.30, and loss factor η = 0.05; and (2) structural steel, commonly used in practical noise barriers, with ρ = 7850 kg/m^3, E = 200 GPa, and v = 0.30. The loss factor was not included in the simulation for structural steel. The material properties of air used in the simulation were: ρ_0 = 1.21 kg/m^3 and sound speed c_0 = 343 m/s.

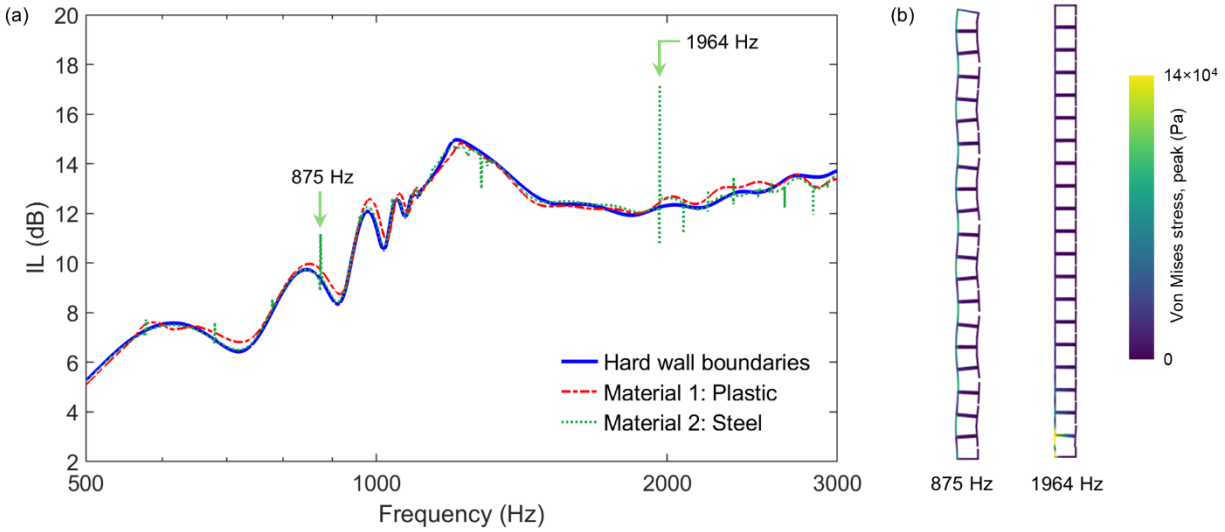

Figure S3. (a) Comparison of insertion loss (IL) obtained using the rigid wall assumption (hard wall boundaries) versus simulations that incorporate the material properties of the noise barrier. Results are shown for two materials: Material 1 (plastic) and Material 2 (steel). (b) Structural deformation of the noise barrier with steel material properties at peak 875 Hz and 1964 Hz. The color scale represents the von Mises stress, and the deformations are exaggerated by scaling factors ranging from 10^3 to 10^5 for visualization purposes.

Figure S3(a) compares the insertion loss (IL) results obtained from the rigid wall assumption with those from the acoustic-structure interaction simulations that include the material properties of the noise barrier. As shown in the figure, the overall IL trends remain consistent across both modelling approaches. It is notable that for 'Material 2: Steel', where material damping (loss factor) was not included, sharp peaks and dips appear in the IL at certain frequencies. These features are attributed to structural resonance modes of the barrier. Figure S3(b) shows the corresponding structural

deformation patterns at frequencies relatively large deviations from the hard-wall boundary case occur.

However, these deviations are relatively minor and do not alter the main conclusions of the study. Furthermore, in practical applications, damping effects are always present, either due to the material itself or through the assembling/installation process. The consistency between the two simulation approaches (rigid wall assumptions and acoustic-structure interaction) confirms that the acoustically rigid assumption is valid for analyzing the key mechanisms underlying the performance of the proposed metabarrier. While the coupled model offers greater physical fidelity, the simplified rigid-wall model employed in the main manuscript effectively captures the essential physics of the system.

S3. Metabarrier response under monopole source excitation

To evaluate the performance of the metabarrier under more realistic excitation conditions, additional numerical simulations were conducted using a monopole (point) sound source placed on the ground surface. This configuration better represents typical traffic noise sources, such as tire-road interactions, which are commonly modeled as near-ground point sources.

Figure S4(a–c) show the simulation setup and results for a monopole source positioned at a horizontal distance of $X_s = H/5$ (0.1 m) from the barrier. The source was placed on the rigid ground, and insertion loss (IL) values were evaluated at receiver positions R_1-R_4, identical to those used in the plane-wave excitation analysis. In the COMSOL Multiphysics simulations, the acoustic source was modeled as a monopole point source with a source strength of $S = 1$ N/m^2. The reference pressure field without the barrier, p_0, was calculated analytically as $p_0 = S\frac{e^{ik_0|\boldsymbol{x}_r-\boldsymbol{x}_s|}}{|\boldsymbol{x}_r-\boldsymbol{x}_s|}$, where $\boldsymbol{x}_r$ and $\boldsymbol{x}_s$ denote the position vectors of the receiver and the source, respectively.

Figure S4(b) and Figure S4(c) indicate that, despite the different source characteristics compared to plane-wave excitation, the metabarrier exhibits similar qualitative behavior, including enhanced attenuation over a broad frequency range and a pronounced peak near the resonance frequency of the Helmholtz resonators. As in the plane-wave case, the enhancement is strongest at receiver positions closest to the barrier and gradually decreases with increasing receiver distance.

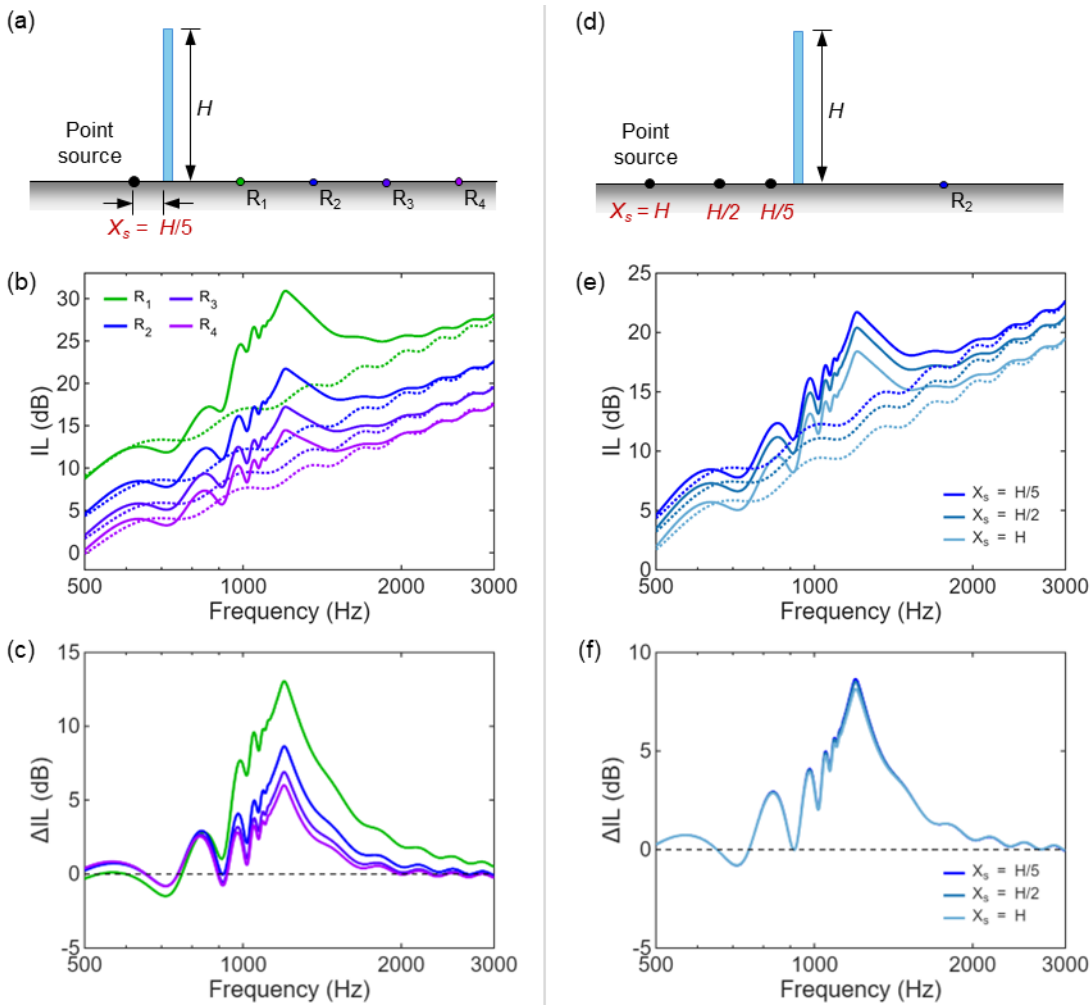

Figure S4. Metabarrier performance under monopole source excitation. (a) Simulation configuration with a ground-based monopole source located at $X_s = H/5$ (0.1 m). (b) Insertion loss (IL) spectra at receiver locations R_1-R_4 for the metabarrier (solid lines) and the plane barrier (dotted lines). (d) corresponding difference in insertion loss (ΔIL). (d) Schematic showing monopole source positions at $X_s = H/5$ (0.1 m), $H/2$ (0.25 m), and H (0.5 m). (e) IL spectra at receiver R_2 for the three source positions. (f) Corresponding ΔIL values.

To further examine the effect of source position, Figure S4(d-f) compares the IL and ΔIL results at receiver location R_2 for three different source distances, $X_s = H/5$ (0.1 m), $H/2$ (0.25 m), and H (0.5 m). As shown in Figure S4(e), the IL values decreases as the source moves farther away from the barrier. However, the corresponding ΔIL curves in Figure S4(f) remain nearly unchanged for the different source positions. This indicates that the relative performance advance of the metabarrier over the plane barrier is largely insensitive to the source-barrier distance within the range considered. These results also demonstrate that the performance enhancement provided by the

metabarrier is not limited to idealized plane-wave excitation, but also persists for monopole sources representative of practical noise scenarios.

S4. Scaling up to realistic noise barrier dimensions

In the main manuscript, the size of the noise barrier was kept relatively small to ensure consistency with the experimental validation. However, the proposed metabarrier design can be readily scaled up while preserving the underlying physical mechanisms. In this section, we demonstrate the noise reduction performance of metabarriers with dimensions representative of realistic outdoor noise barriers.

Figure S5 presents numerical simulation results for scaled-up metabarriers with a total height of 3 m. Note that conventional noise barriers typically range in height from 2 to 6 meters, with 3 to 4 meters being common in urban highway settings. In all cases, insertion loss (IL) values were calculated at four receiver positions (R_1-R_4) located at distances ranging from 1.5 m to 6.0 m from the right-hand side of the barrier, with a spacing of 1.5 m. For reference, the IL of a conventional plane barrier with identical overall dimensions is also included (dotted lines).

Figure S5(a) and (b) show the results for a metabarrier with a total height of 3 m, width of 150 mm, and 20 unit cells, each having a square cross-section of 150 mm × 150 mm. This configuration corresponds to a direct geometric scaling (by a factor of six) of the baseline design presented in Figure 2 of the main manuscript. In the scaled model, each resonator has a side length of d = 150 mm, the wall thickness t_p = 12 mm, internal cavity side length d_i = 126 mm, and the neck width a = 6 mm. The results demonstrate that the overall IL trends of the scaled-up metabarrier closely resemble those observed in the smaller-scale version discussed in the main manuscript. Notably, the frequency range of attenuation has shifted to lower frequencies due to the increased physical dimensions of the resonators, with the primary resonance occurring around 200 Hz.

Figure S5(c) and (d) present a second configuration in which the resonator cross-section is reduced to 150 mm × 100 mm, while maintaining the same total barrier height. To compensate for the reduced unit height, 30 unit cells were stacked vertically. Due to the smaller internal cavity volume

of the unit resonator, the resonance frequency shifts to higher frequencies, along with the peaks associated with surface-wave modes.

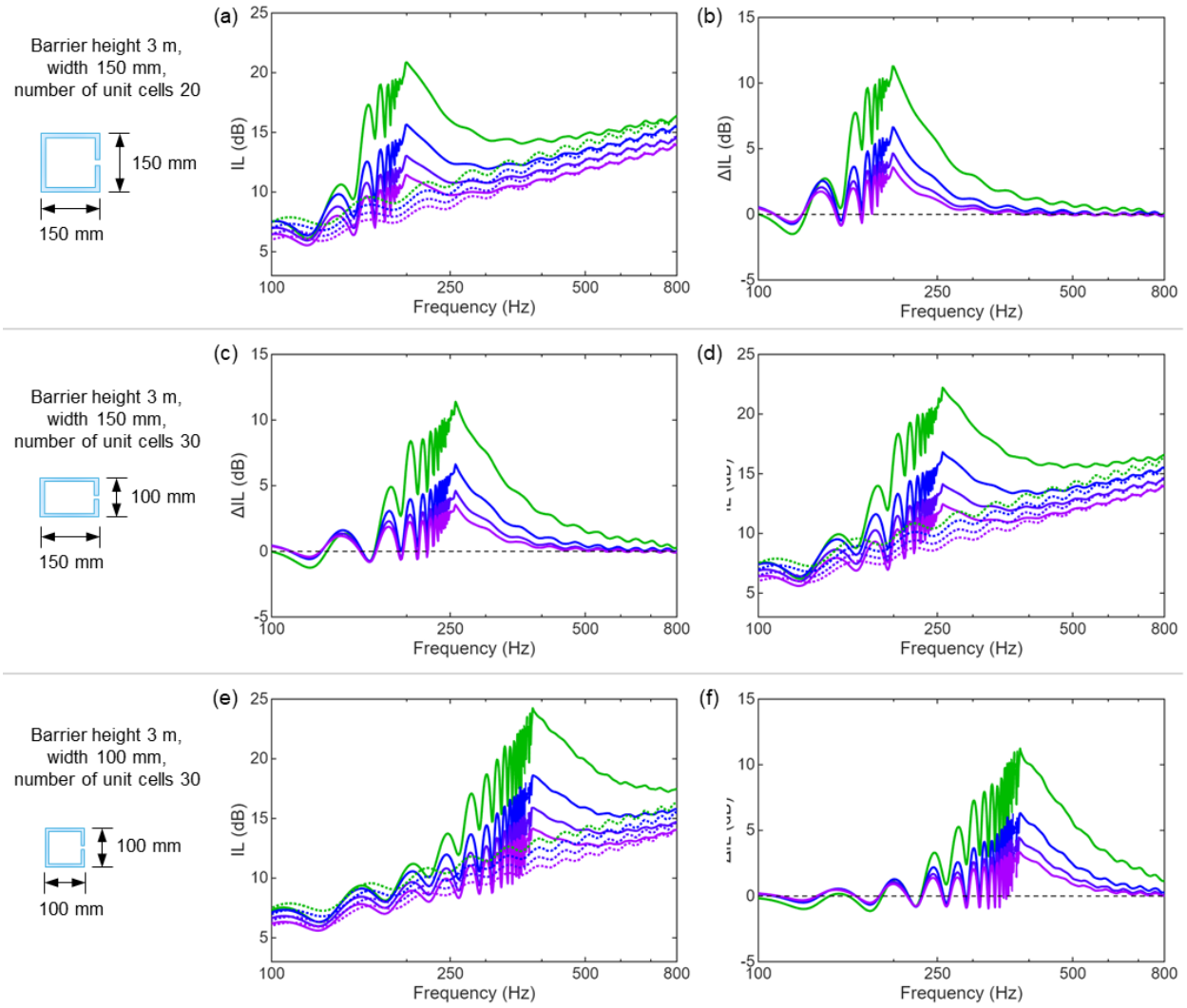

Figure S5. Insertion loss (IL) and IL difference (ΔIL) for metabarriers with realistic dimensions targeting traffic-noise frequencies. (a,b) Barrier height 3 m, width 150 mm, 20 unit cells with resonator cross-section 150 mm × 150 mm. (c,d) Barrier height 3 m, width 150 mm, 30 unit cells with resonator cross-section 150 mm × 100 mm. (e,f) Barrier height 3 m, width 100 mm, 30 unit cells with resonator cross-section 100 mm × 100 mm. Solid lines indicate metabarriers, and dotted lines indicate plane barriers of identical dimensions.

While maintaining the total barrier height and the number of resonators, the frequency response can also be tuned by modifying the barrier width. Figure S5(e) and (f) show the results for a more compact design with a barrier width of 100 mm and 30 unit cells of size 100 mm × 100 mm.

Similar to the configuration shown in Figure S5(c) and (d), the overall response shifts to higher frequencies as a result of the increased resonance frequency of the individual resonator units.

Overall, these results confirm that the proposed metabarrier design is readily adaptable to realistic dimensions and target frequency ranges. Since the resonance frequency of each Helmholtz resonator is primarily determined by its geometric parameters, the metabarrier design is highly adaptable to various acoustic environments. Although frequency tuning is demonstrated here by varying the resonator size, it can also be readily achieved by adjusting the neck width (a) or other geometric parameters, as discussed in the main manuscript. In addition, employing double-array resonator configurations, as demonstrated in Section 4 of the main manuscript, provides a further strategy for broadening the effective attenuation bandwidth.

S5. Comparison with other metamaterial designs

We note that a direct comparison of the acoustic performance of the proposed metamaterial noise barrier with previously developed metamaterials is not feasible, as, to the best of the authors' knowledge, no prior studies have addressed the same acoustic problem setting. Although a large body of research has been devoted to developing metamaterials for noise reduction [1, 2], they were developed for acoustic configurations where edge diffraction over the finite height of the entire system is not taken into account. Thus, a direct comparison is not appropriate, as those metamaterials were specifically designed for different objectives, rather than for noise barrier configurations where wave diffraction plays a critical role.

Nevertheless, it is worth noting that the Helmholtz resonators employed in this study achieve a considerably broad effective frequency range, when compared to several recently proposed metamaterials, as summarized in Table S1. We again emphasize that the applications of these other metamaterial studies differ from ours; therefore, direct comparison is not suitable. The information provided in Table S1 is intended solely to offer additional context regarding relative performance characteristics, rather than to imply direct equivalence or competition.

Table S1. Comparison of the resonator and effective frequency range of this work with other types of metamaterials reported in the literature. The symbol W denotes the total thickness of the structure, f_r represents the (first) resonance frequency, and λ_r is the corresponding wavelength. The frequency range shown in parentheses below f_r indicates the frequency range over which improved performance is achieved. The ratio λ_r/W quantifies the compactness of the resonator relative to its thickness, with higher values indicating more compact (thinner) designs.

Reference	W (mm)	f_r (Hz)	λ_r/W	Resonator type; application
This work (single-array case)	25	1203 (750-2000)	11.40	Helmholtz resonator; Noise barrier
Xu et al. (2024) [3]	100	860 (770-1768)	4.45	Open coiled-up channel; Ventilated sound insulation
Zhu et al. (2022) [4]	100	600 (600-1900)	5.72	Open coiled-up channel; Ventilated sound insulation
Wu et al. (2021) [5]	100	1600 (1600-1900)	2.14	Closed coiled-up channel; Ventilated sound insulation
Jang et al. (2022) [6]	12.5	2120 (multiple frequency ranges above 2000)	12.94	Membrane with cavity; Sound insulation
Yang et al. (2024) [7]	70	360 (Not specified)	13.61	Helmholtz resonator; Reducing sound radiation of an enclosure with opening
Yang et al. (2024) [8]	75	660 (500-3000)	6.93	Microperforated panel; Reducing sound radiation of a duct with opening

S6. Far-field response

To evaluate the far-field response of the metabarrier, numerical simulations were performed using an enlarged air domain. In these simulations, insertion loss (IL) values were calculated at receiver locations ranging from H (= 0.5 m) to $10H$ (= 5 m) from the barrier, with an interval of H. For comparison, the same simulations were conducted for a conventional plane barrier with identical height.

Figure S6(a) and (b) compare the acoustic pressure fields around the metabarrier and plane barrier at 1203 Hz, corresponding to the primary resonance frequency of the Helmholtz resonators. Near the barrier, the metabarrier noticeably alters the diffracted wave field. However, as the wave propagates farther away from the barrier, the pressure fields of the two configurations become increasingly similar, indicating that the influence of the resonator array diminishes with distance.

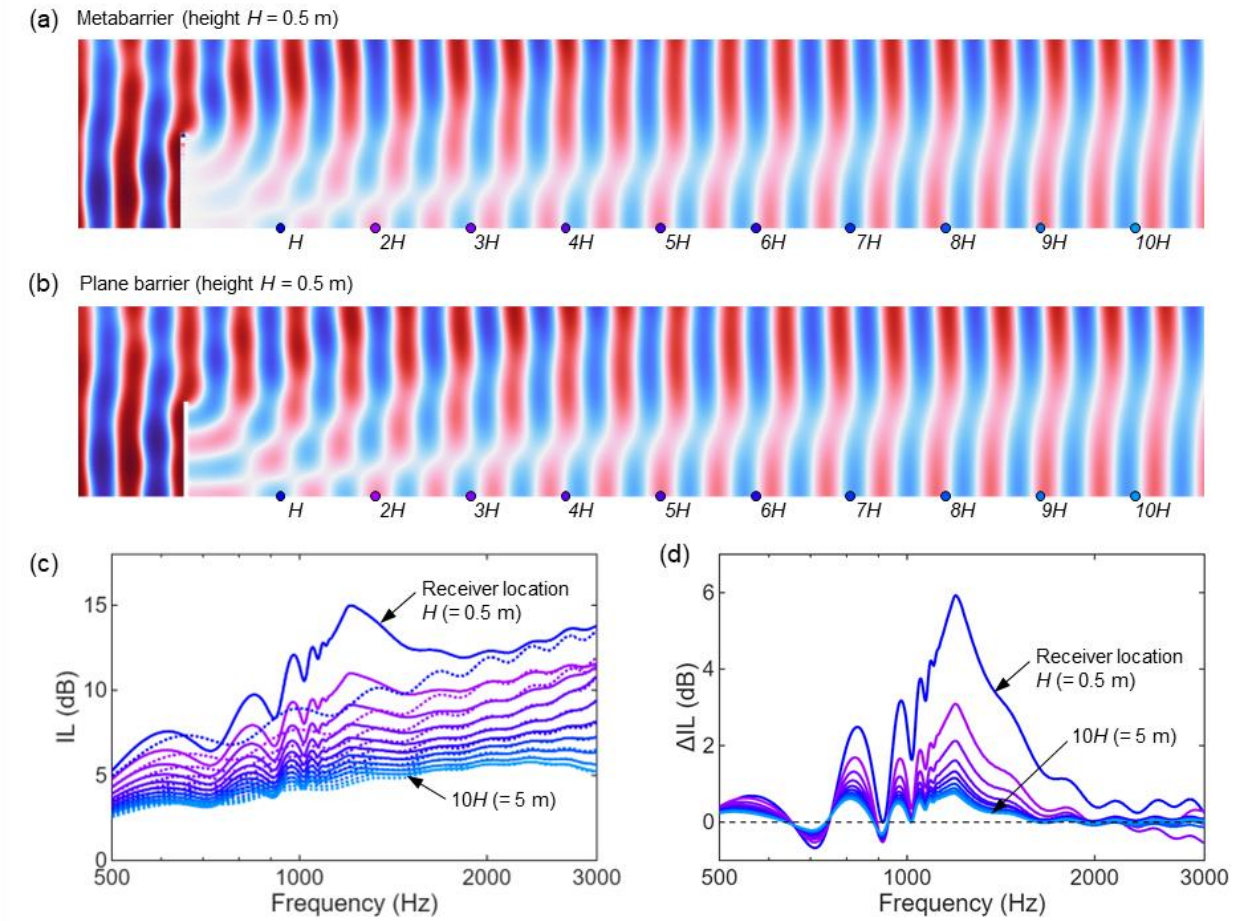

Figure S6. Far-field response of the metabarrier compared with a plane barrier. (a) Acoustic pressure field at 1203 Hz for the metabarrier (height H = 0.5 m) in an extended simulation domain. (b) Acoustic pressure field at 1203 Hz for a plane barrier of the same height. Receiver locations are indicated from H to 10H along the ground. (c) Insertion loss (IL) spectra calculated at receiver locations ranging from H (= 0.5 m) to 10H (= 5 m) for the metabarrier (solid lines) and the plane barrier (dotted lines). (d) Difference in insertion loss (ΔIL) between the metabarrier and the plane barrier at the same receiver locations.

Figure S6(c) presents the IL spectra calculated at all receiver locations for the metabarrier (solid lines) and the plane barrier (dotted lines). The IL decreases substantially with increasing receiver distance for both barriers. Although higher IL values are observed close to the metabarrier, this enhancement progressively weakens as the receiver moves farther away. The corresponding IL difference, ΔIL, between the metabarrier and the plane barrier is shown in Figure S6(d). The results demonstrate that the additional attenuation provided by the metabarrier is mainly effective at closer distances. At larger distances (e.g., 8H-10H), the ΔIL values approach zero over most of the frequency range, with only minor residual enhancement around 1 dB near the resonance frequency.

Overall, these results indicate that while the metabarrier is effective in modifying the diffracted wave field and enhancing sound attenuation close to the barrier, its advantage over a conventional plane barrier becomes limited in the far field. This behavior is consistent with the localized nature of the underlying attenuation mechanisms, which primarily act near the barrier edge. While the present metabarrier primarily affects the near-field diffraction behavior, it may be integrated with barrier designs that target far-field noise reduction. Such hybrid approaches could combine the diffraction-modifying capability of the metabarrier with established far-field attenuation mechanisms, potentially enhancing overall noise-barrier performance.

S7. Single array of resonators alternatively facing opposite sides

In Section 4 of the main manuscript, we presented the analysis of metabarriers with double-array resonators that have the overall barrier width $2W$. Alternatively, one can maintain the same barrier width as W and arrange resonators alternately facing opposite sides, as shown in the left-hand figure of Figure S7(g). The width and total height of the barrier remain unchanged, with 10 alternating-resonator units stacked on top of each other. In this configuration, the performance of the noise barrier results from the combined effects of the two sub-units, as depicted in the middle and right-hand figures of Figure S7(g). Figure S7(a), (b), and (c) present the ILs of such metabarriers, varying the resonator neck width of the resonators facing the left-hand side (a_2) at 1 mm, 2 mm, and 3 mm, while keeping the neck width of the resonators facing the right-hand side (a_1) fixed at 1 mm. The ΔIL values and contributions of the sub-units are shown in Figure S7(d), (e), and (f).

The results indicate that, similar to the double-array metabarriers, alternating the orientation of the resonators produces a cumulative sound attenuation effect from each sub-unit, as observed in the ΔIL graphs. The highest peak IL calculated at R_1 in Figure S7(a) is 20.60 dB, which is higher than that of the original single-array design. This configuration capitalizes on the advantages of both resonator orientations while maintaining the overall barrier width. However, it is important to note that the frequency ranges of enhanced IL are narrower compared to those of the original single-array or double-array metabarriers.

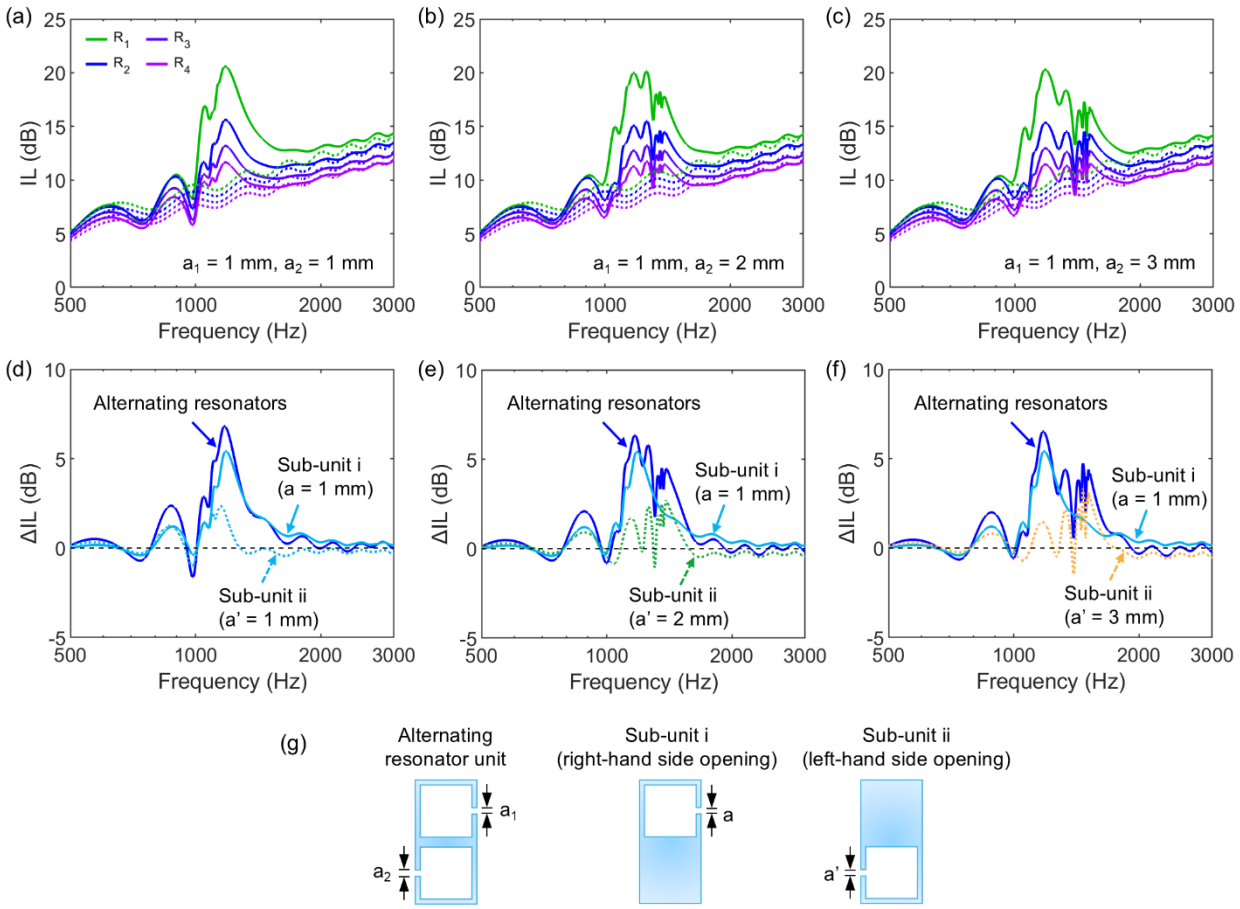

Figure S7. Sound attenuation by single-array metabarrier with resonators alternatively facing opposite sides. Insertion losses by the metabarriers with resonator neck widths (a) a_1 = 1 mm, a_2 = 1 mm, (b) a_1 = 1 mm, a_2 = 2 mm, and (c) a_1 = 1 mm, a_2 = 3 mm. The difference of insertion losses between the metabarriers and plane barriers are shown in (d), (e), and (f) for the configurations considered in (a), (b), and (c), respectively. (g) Configurations of alternating resonator unit (left), sub-unit *i* (middle), and sub-unit *ii* (right).

References

[1] N. Gao, Z. Zhang, J. Deng, X. Guo, B. Cheng, and H. Hou, "Acoustic Metamaterials for Noise Reduction: A Review," *Adv. Mater. Technol.*, vol. 7, no. 6, p. 2100698, 2022, doi: 10.1002/admt.202100698.

[2] A. Arjunan, A. Baroutaji, J. Robinson, A. Vance, and A. Arafat, "Acoustic metamaterials for sound absorption and insulation in buildings," *Build. Environ.*, vol. 251, p. 111250, Mar. 2024, doi: 10.1016/j.buildenv.2024.111250.

[3] Z. Xu, W. Qiu, Z. Cheng, J. Yang, B. Liang, and J. Cheng, "Broadband ventilated sound insulation based on acoustic consecutive multiple Fano resonances," *Phys. Rev. Appl.*, vol. 21, no. 4, p. 044049, Apr. 2024, doi: 10.1103/PhysRevApplied.21.044049.

[4] Y. Zhu, R. Dong, D. Mao, X. Wang, and Y. Li, "Nonlocal Ventilating Metasurfaces," *Phys. Rev. Appl.*, vol. 19, no. 1, p. 014067, Jan. 2023, doi: 10.1103/PhysRevApplied.19.014067.

[5] H. W. Wu, Y. Q. Yin, Z. Q. Sheng, Y. Li, D. X. Qi, and R. W. Peng, "Multiband omnidirectional ventilated acoustic barriers based on localized acoustic rainbow trapping," *Phys. Rev. Appl.*, vol. 15, no. 5, p. 54033, 2021, doi: 10.1103/PhysRevApplied.15.054033.

[6] J.-Y. Jang, C.-S. Park, and K. Song, "Lightweight soundproofing membrane acoustic metamaterial for broadband sound insulation," *Mech. Syst. Signal Process.*, vol. 178, p. 109270, Oct. 2022, doi: 10.1016/j.ymssp.2022.109270.

[7] E. Yang, J. Kim, and W. Jeon, "Complex-valued impedance tiles to reduce noise emanating through openings in mechanical systems," *Mech. Syst. Signal Process.*, vol. 209, p. 111054, Mar. 2024, doi: 10.1016/j.ymssp.2023.111054.

[8] W. Yang, Y. Li, and Y. S. Choy, "Sound radiation control of an unbaffled long enclosure using wavy micro-perforated panel absorbers," *J. Sound Vib.*, vol. 574, p. 118233, Mar. 2024, doi: 10.1016/j.jsv.2023.118233.